Journal of Colloid and Interface Science 344 (2010) 353–361

Contents lists available at ScienceDirect

Journal of Colloid and Interface Science

www.elsevier.com/locate/jcis

Three-dimensional off-lattice Monte Carlo simulations on a direct relation between experimental process parameters and fractal dimension of colloidal aggregates

Songkil Kim [a], Kwang-Sung Lee [a], Michael R. Zachariah [b,c], Donggeun Lee [a,*]

[a] School of Mechanical Engineering, Pusan National University, Busan 609-735, Republic of Korea
[b] Department of Mechanical Engineering, University of Maryland, MD 20742, USA
[c] Department of Chemistry and Biochemistry, University of Maryland, MD 20742, USA

ARTICLE INFO

Article history:
Received 7 November 2009
Accepted 7 January 2010
Available online 14 January 2010

Keywords:
Monte Carlo simulation
Aggregation
Fractal structure
Suspension stability

ABSTRACT

It has been a big challenge to explore a direct relation of experimental parameters such as pH, electrolyte concentration, particle size, and temperature with the final structures of aggregates, because Monte Carlo simulations have been performed on the basis of arbitrarily chosen sticking probability. We attempted to incorporate colloidal theory to Monte Carlo simulations for two model systems of CuO– and SiO_2–water systems, so as to resolve this difficulty. Conducting three-dimensional off-lattice MC simulations at various pHs for both systems, we investigated effects of pH on fractal structures of aggregates, encompassing the whole aggregation regime from diffusion-limited cluster–cluster aggregation to reaction-limited cluster–cluster aggregation. Moreover, developing a functional analysis, we found an explicit correlation between experimental parameters, sticking probability, and the fractal dimension of aggregates for both systems.

1. Introduction

Control of aggregation of particles in a gas or a liquid is of great interest in a variety of applications. For example, severe aggregation of particles during sol–gel reaction [1] or flame aerosol synthesis [2–5] should be avoided for the purposes of sintering [2] and nanotherapeutics [6]. Fractal-like aggregates, when they are compacted and sintered to form a bulk solid, often make internal pores bigger and non-uniform, causing a sudden grain growth at the final stage of sintering [2]. Aggregation also leads to polydispersity of produced nanoparticles, hampering their application to nanotherapeutics in human [6]. On the other hand, open-structured aggregates can often offer benefits to enhance energy transfer in nanofluids due to the percolation effect on heat transfer [7,8] or to reduce heat transfer rate as a thermal insulator by constituting porous aerogel structures [9], and as catalytic electrodes with lowered electrical resistance in fuel cells [10]. The control of aggregation is thus critical to many applications and provides the impetus for better predicative capabilities.

Many approaches have been developed to simulate aggregation. Monte Carlo (MC) simulation offers some benefits in enabling to predict both the evolution of the aggregate structure and the aggregation kinetics [11–19]. Recently, three-dimensional off-lattice MC simulation method has been preferred rather than on-lattice MC simulation because a random directional movement of particle is not restricted to lattice sites [16]. Hence, the term of MC simulation that will be used hereafter represents the three-dimensional off-lattice MC simulation method unless otherwise noted. Brownian dynamics simulation [20,21], while offering similar benefits, requires much longer computation time. While population balance equations [22,23], which is computationally more efficient for simulating the aggregation kinetics, does not provide any information on aggregate connectivity. MC simulations are particularly useful in tracking the different regimes of aggregation, i.e., diffusion-limited cluster–cluster aggregation (DLCA), or reaction-limited cluster–cluster aggregation (RLCA) [24–26]. Traditionally, however, MC simulations reveal that the geometrical characteristics of aggregates described by the fractal dimension (d_f) are highly model-dependent, for example, the d_f of 1.75–1.8 for the DLCA and d_f of 2.1–2.2 for the RLCA [11–18,24–26].

The DLCA and the RLCA represent two limiting regimes and evolve by the efficiency of collision, i.e., the average number of collisions for permanent inter-particle bonding, that can be expressed as a sticking probability (P_{ij}) in the range of 0–1. Close to unity, each collision yields growth of the aggregates, so that the overall growth rate approaches that of the diffusive flux and represents the DLCA regime. For P_{ij} near zero (RLCA), most collisions are reflective which enables the monomer to skip from one site to another, and penetrate deeper within the aggregate to make a denser

* Corresponding author. Fax: +82 51 512 5236.
E-mail address: donglee@pusan.ac.kr (D. Lee).

0021-9797/$ - see front matter © 2010 Elsevier Inc. All rights reserved.
doi:10.1016/j.jcis.2010.01.008

structure. It should be noted however that while MC simulations seemingly imply the ability to predict aggregate structure, the key parameter of P_{ij} should be known as an input parameter prior to the simulation. For this reason, the majority of previous MC simulation studies were made on the basis of an arbitrarily chosen probability. As such, MC has not found use in the simulation of real world systems where the operational parameters to control aggregation are process parameters, e.g., pH, electrolyte concentration, and temperature. How these parameters connect to the sticking probability used in MC simulation is thus a key point.

In this study, we employ both a surface complexation model and Derjaguin–Landau–Verwey–Overbeek (DLVO) theory [1,7,27,28] to provide the linkage between experimental process parameters and the P_{ij} values, via consecutive calculations of surface charge states, total interaction potential between particles, anti-collision or suspension stability of particles. Two model systems of CuO– and SiO_2–water was chosen to apply this process, because aggregation control is of great importance in many application fields [29–31], and electrokinetic parameters of the two materials are well known but contrasted, making the current analysis quite appropriate in a wide range [1,32,33]. By performing three-dimensional off-lattice MC simulations as a function of pH for both systems, we investigated effects of pH on the fractal structures of aggregates, encompassing the whole aggregation regime from DLCA-to-RLCA. Finally, we find an explicit correlation between experimental parameters and the fractal dimension of particles for both systems.

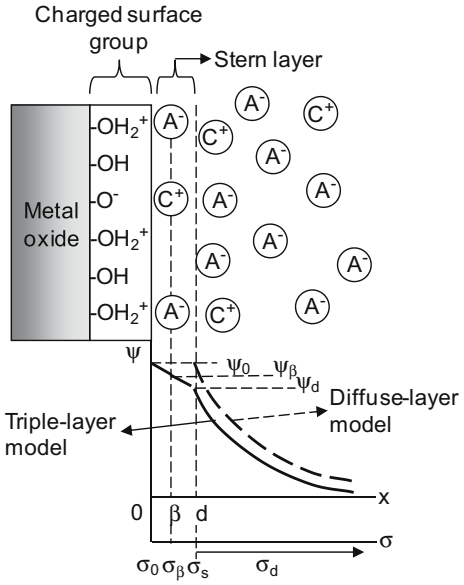

Fig. 1. Structure of electrical double layer (EDL) formed at the metal oxide–water interface[14,22]: counter ion A^- or C^+ bonded strongly to the charged group at surface forms an immobile part of the EDL (stern layer). In contrast, in the outer region named as a diffuse layer, such ions are bound weakly, resulting in gradual decrease in the potential. The σ_0, σ_β, and σ_d are charge densities at the surface (0-plane), inner-Hermholtz plane, and in the diffuse layer, respectively.

2. Surface charge states and inter-particle potentials

2.1. Surface complexation model

When solid particles such as oxides, sulfides, and insoluble salts are immersed in aqueous solution, they acquire a surface charge due to protonation or deprotonation of surface groups such as the hydroxyl ligand (–OH) of the metal oxide as follows [1,7,27]:

$$\begin{aligned} &\mathrm{MOH} + \mathrm{H^+} \underset{K_p}{\rightarrow} \mathrm{MOH_2^+}, \quad K_p = \exp\left(\frac{F\psi_0}{RT}\right)\frac{\Gamma(\mathrm{MOH_2^+})}{a(\mathrm{H^+})\Gamma(\mathrm{MOH})} \\ &\mathrm{MOH} \underset{K_d}{\rightarrow} \mathrm{MO^-} + \mathrm{H^+}, \quad K_d = \exp\left(-\frac{F\psi_0}{RT}\right)\frac{\Gamma(\mathrm{MO^-})a(\mathrm{H^+})}{\Gamma(\mathrm{MOH})} \end{aligned} \tag{1}$$

where M is a metal cation, i.e. Cu^{2+} and Si^{4+} in this case, K_p and K_d are intrinsic equilibrium constants for protonation and deprotonation, respectively, a is activity in the bulk of the solution, ψ_0 is surface potential affecting the number of charged surface groups MOH_2^+ and MO^-, Γ is a site density of the surface groups, R is the gas constant, and T is absolute temperature. The equilibrium constants are not independent each other, but interrelated through the point of zero charge (PZC) of particles in water [1].

$$\mathrm{PZC} = \frac{1}{2}\log\left(\frac{K_p}{K_d}\right) \tag{2}$$

Counter ions with opposite polarity in the electrolyte are attracted to the charged surface groups, resulting in a decrease of the potential in the stern layer ($0 < x < d$) in Fig. 1. The adsorption of the counter ions is expressed by

$$\begin{aligned} &\mathrm{MOH_2^+} + \mathrm{A^-} \underset{K_a}{\rightarrow} \mathrm{MOH_2^+ \cdot A^-}: \quad K_a = \exp\left(-\frac{F\psi_\beta}{\mathrm{RT}}\right)\frac{\Gamma(\mathrm{MOH_2^+ \cdot A^-})}{a(\mathrm{A^-})\Gamma^*(\mathrm{MOH_2^+})} \\ &\mathrm{MO^-C^+} \underset{K_c}{\rightarrow} \mathrm{MO^- \cdot C^+}: \quad K_c = \exp\left(\frac{F\psi_\beta}{\mathrm{RT}}\right)\frac{\Gamma(\mathrm{MO^- \cdot C^+})}{a(\mathrm{C^+})\Gamma^*(\mathrm{MO^-})} \end{aligned} \tag{3}$$

where as a symmetric 1:1 electrolyte $(NaCl)_{aq}$ of 5×10^{-4} mol dm^{-3} (far less than the critical coagulation concentration of 5×10^{-2} mol dm^{-3}) was used in this study, A^- and C^+ correspond to Cl^- and Na^+, respectively, and K_a and K_c are the equilibrium constants for surface adsorption of the anion and the cation, respectively. Note that some of the parent charged sites of $\Gamma(MOH_2^+)$ and $\Gamma(MO^-)$ in Eq. (1) subsequently associate counter ions so that the remainder of $\Gamma^*(MOH_2^+)$ and $\Gamma^*(MO^-)$ are second equilibrated with $\Gamma(MOH_2^+ \cdot A^-)$, and $\Gamma(MO^- \cdot C^+)$. Rearranging the terms in Eqs. (1) and (3), the four charged site densities are expressed as a function of uncharged site density $\Gamma(MOH)$. The total sum of charged and uncharged site densities is equal to the total surface site density Γ_{tot} (ca. 5.88×10^{-6} mol m^{-2} for CuO [27] and 7.60×10^{-6} mol m^{-2} for SiO_2 [34]). Using this, one can readily derive the following equations

$$\begin{aligned} \frac{\Gamma_{\mathrm{tot}}}{\Gamma(\mathrm{MOH})} &= 1 + \frac{K_p a_s(\mathrm{H^+})}{1 + K_a a_\beta(\mathrm{A^-})} + \frac{K_d/a_s(\mathrm{H^+})}{1 + K_c a_\beta(\mathrm{C^+})} \\ &\quad + \frac{K_a K_p a_s(\mathrm{H^+}) a_\beta(\mathrm{A^-})}{1 + K_a a_\beta(\mathrm{A^-})} + \frac{K_c K_d a_\beta(\mathrm{C^+})/a_s(\mathrm{H^+})}{1 + K_c a_\beta(\mathrm{C^+})} \\ &= 1 + a_s(\mathrm{H^+})K_p + K_d/a_s(\mathrm{H^+}) \end{aligned} \tag{4}$$

where the activity of H^+ at the surface and activities of C^+ and A^- at the β-plane (the inner Helmholtz plane) are given by Maxwell–Boltzman distribution [1] as

$$\begin{aligned} &a_s(\mathrm{H^+}) \equiv a(\mathrm{H^+})\exp\left(-\frac{F\psi_0}{RT}\right), \quad a_\beta(\mathrm{C^+}) \equiv a(\mathrm{C^+})\exp\left(-\frac{F\psi_\beta}{RT}\right), \\ &a_\beta(\mathrm{A^-}) \equiv a(\mathrm{A^-})\exp\left(\frac{F\psi_\beta}{RT}\right) \end{aligned} \tag{5}$$

The potential ψ_β at the β-plane in Eq. (5) is often approximated to the surface potential ψ_0 for electrolyte ions adsorbed *non-specifically*, which is the case for this study. It is also known that the ψ_0 is reasonably approximated to the Nernst potential ψ_N (= $\log[a(H^+)/a_{pzc}(H^+)]RT/F$) with 90% accuracy [1]. The charge densities in 0- and β-planes (σ_0 and σ_β) are given by definition as

$$\begin{aligned} \sigma_0 &= F[\Gamma(\mathrm{MOH_2^+}) - \Gamma(\mathrm{MO^-})] = F[\Gamma^*(\mathrm{MOH_2^+}) + \Gamma(\mathrm{MOH_2^+ \cdot A^-}) \\ &\quad - \Gamma^*(\mathrm{MO^-}) - \Gamma(\mathrm{MO^- \cdot C^+})] \end{aligned} \tag{6}$$

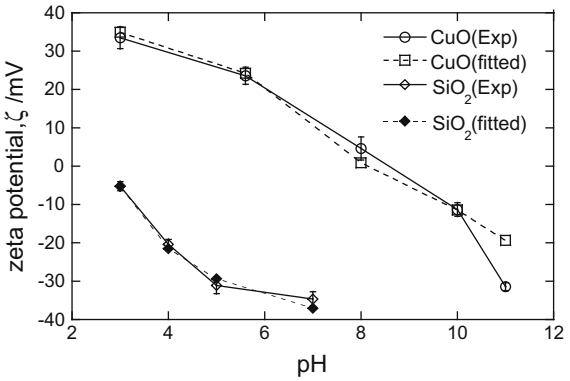

Fig. 2. Comparison of measurements and model predictions of zeta potentials for CuO– and SiO_2–water systems at various pHs.

$$\sigma_\beta = F[\Gamma(\mathrm{MO^-}\cdot\mathrm{C^+}) - \Gamma(\mathrm{MOH_2^+}\cdot\mathrm{A^-})] \tag{7}$$

The sum of the two charge densities, or so-called net surface charge σ_s, is balanced with that in the diffusive layer σ_d (refer to Fig. 1) as

$$\sigma_s = \sigma_0 + \sigma_\beta = F[\Gamma^*(\mathrm{MOH_2^+}) - \Gamma^*(\mathrm{MO^-})] = -\sigma_d = -\frac{4000FI}{\kappa}\sinh\left(\frac{F\psi_d}{2RT}\right) \tag{8}$$

where I is ionic strength in the units of mol dm^{-3}, F is Faradays constant (96,485 C mol^{-1}), and the reciprocal Debye–Huckel parameter κ^{-1} ($=\sqrt{\varepsilon_0\varepsilon_r RT/2000F^2I}$) often scales as the thickness of the electrical double layer. Hunter [1] suggested that the electrokinetic or zeta potential (ζ) measured the electrostatic potential at, or very near to, the beginning of the diffuse layer ($\psi_d \approx \zeta$) [1]. Hence, starting with the approximation of $\psi_0 \approx \psi_N$, the activities of $a_s(H^+)$, $a_\beta(A^-)$, and $a_\beta(C^+)$ are estimated using Eq. (5). Together with initial guesses of K_p, K_d, K_a, and K_c, the activities and potentials are applied to Eq. (4), so as to obtain the Γ(MOH). It is fairly straightforward to calculate all the charged site densities by using Eqs. (1) and (3). Then, Eqs. (6)–(8) give the surface charge densities of σ_0, σ_β, σ_s, and σ_d, leading to update of ψ_d approximating ζ. This process is repeated with different values of the four equilibrium constants until the estimated ζ gets closest to the measured value at different pHs.

Fig. 2 shows the variations of ζ potentials measured for SiO_2– and CuO–water systems at various pHs, in comparison with the best-fitted profiles depicted with dotted lines. Details for the measurement of ζ potentials were described in our previous publication [27]. All parameters used for the best fit are listed in Table 1. To verify this model, the values of 0.5 $\log(K_p/K_d)$ for both systems are calculated from the parameters in Table 1 and then compared with the PZC values from literature [1,32,33]: the calculated values of 8.12 and 2.05 for CuO and SiO_2 systems are both in good agreements with the literature values of 8–9 and 2–2.5, respectively.

Table 1
Parameters used for the estimation of the ζ potential.

	CuO	SiO_2
K_p/mol^{-1} dm^3	1.8×10^{4}	1.5×10^{-1}
K_d/mol^{-1} dm^3	9.0×10^{-13}	1.2×10^{-5}
K_a/mol^{-1} dm^3	58	1
K_c/mol^{-1} dm^3	1	2550
Γ_{tot}/mol^{-1} dm^3	5.88×10^{-6}	7.64×10^{-6}
T/K	298	
R/J mol^{-1} K^{-1}	8.31	
ε_0/C V^{-1} m^{-1}	8.854×10^{-12}	
ε_r for water	80	

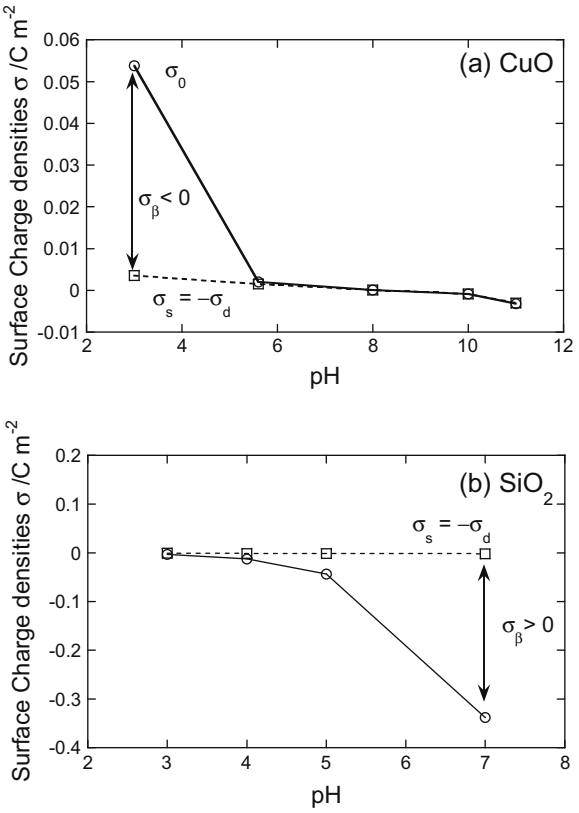

Fig. 3. Surface charge densities of: (a) CuO and (b) SiO_2 nanoparticles in the aqueous solution at various pHs.

Fig. 3 shows that the surface charge density σ_0 is in fairly close agreement to the net surface charge density σ_s (= $-\sigma_d$) unless the pH is far from the PZC, which is particularly true in the case of CuO. This suggests that the effect of surface association by counter ions might be insignificant at $-3.0 < \Delta pH\ (\equiv pH - PZC) < 3.0$. The region of ΔpH corresponds to transition region between DLCA and RLCA that is of particular interest in this study and will be shown later.

2.2. Inter-particle potentials and suspension stability

According to DLVO theory which describes the stability of colloids [7,21,27,28], particles in liquid suspension repel or attract each other depending on the total interaction energy U_{tot} which is the sum of electrical repulsion energy U^{el} and van der Waals attraction energy U^{vdW}. Verwey and Overbeek (1948) [1] showed that a very good approximation of the U^{el} between two identical flat surfaces, valid for all potentials, would be

$$U^{el}(\text{flat plate}) = 32\frac{\varepsilon_0\varepsilon_r R^2T^2}{F^2z^2}Z^2\left[1-\tanh\left(\frac{\kappa x}{2}\right)\right] \tag{9}$$

in the case of a weak overlapping of the double layers, where z is the charge of the solvated ions (= 1.0 in this study) and $Z \equiv \tanh[zF\psi_d/(4RT)]$. For two identical spherical particles approaching each other under the constant potential condition, the repulsion energy U^{el} is calculated by applying Deryaguin approximation [1] to Eq. (9) as

$$U^{el} = \int_x^\infty U^{el}(\text{flat plate})dx = 32\pi r\frac{\varepsilon_0\varepsilon_r R^2T^2}{F^2z^2}Z^2\ln[1+\exp(-\kappa x)] \tag{10}$$

where r is particle radius, and x is the surface-to-surface distance between the two particles. For small potentials ($F\psi_d \leqslant 2RT$), since Z is well approximated by $zF\psi_d/(4RT)$, Eq. (10) reduces to the following popular equation:

$$U^{el} \approx 2\pi\varepsilon_0\varepsilon_r r\psi_d^2 \ln[1+\exp(-\kappa x)] \propto \psi_d^2 \quad (11)$$

Thus, it is obvious that the higher the surface potential, the more stable the colloid, due to the higher electrical repulsion energy. If the value of $F\psi_d$ increases over $4RT$, one has to be careful in using Eq. (11) because the repulsion energy U^{el} is overestimated by Eq. (11) due to the nature of the hyperbolic tangent function in Z. Therefore, Eq. (10) should be used at high surface potential. The van der Waals attraction energy between adjacent particles is given under Derjaguin approximation in the non-retarded limit by [1,6,7,21,27,28]

$$U^{vdW} = -\frac{A_{132} r}{12x} \quad (12)$$

where A_{132} is the Hamaker constant of 4.6×10^{-21} J and 2.0×10^{-20} J for SiO_2– and CuO–water systems, respectively [1,21,27,35].

Applying the parameters in Table 1 and the results in Figs. 2 and 3, the total interaction energy U_{tot} defined as the sum of U^{el} and U^{vdw} are calculated as a function of the distance between two particles, x, and is shown for both colloidal systems in Fig. 4. Recalling the PZC of 8.12 for the CuO–water system, Fig. 4a shows that the maximum of the total interaction energy representing the repulsion energy barrier ($U_{tot,max}$) increases as pH goes far from the PZC, leading to more stable colloidal system. In Fig. 4b, SiO_2 particles exhibit a similar behavior of the $U_{tot,max}$ when increasing pH from the PZC of 2.05. Note that the highest value of $U_{tot,max}$ in CuO–water system ($\sim$7.3 k_bT at ΔpH = −5.12) is a little smaller than that in the SiO_2–water system ($\sim$8.3 k_bT at ΔpH = 4.95).

The higher energy barrier in SiO_2–water system is attributed to a smaller contribution of the attraction energy U^{vdW} to lowering the energy barrier due to the smaller Hamaker constant (see Table 1). Fig. 4a also shows that the x value at which U_{tot} is maximum (x_{max}) gradually increases from 2.7 nm to $\sim$7.7 nm as pH approaches PZC. At pH 8 closest to PZC, the total interaction energy is negative at the entire region of x. In a stable colloidal system, U_{tot} is dominated by the positive

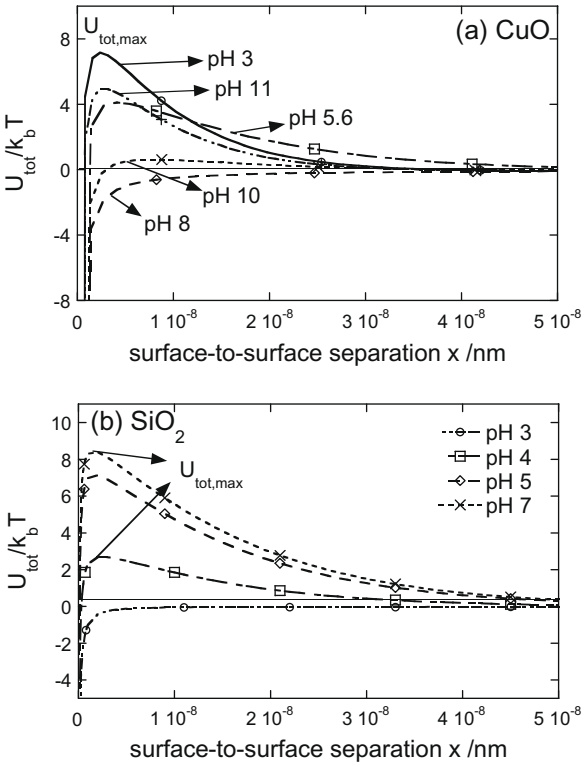

Fig. 4. Total interaction potentials of: (a) CuO and (b) SiO_2 nanoparticles as a function of inter-particle distance at various pHs.

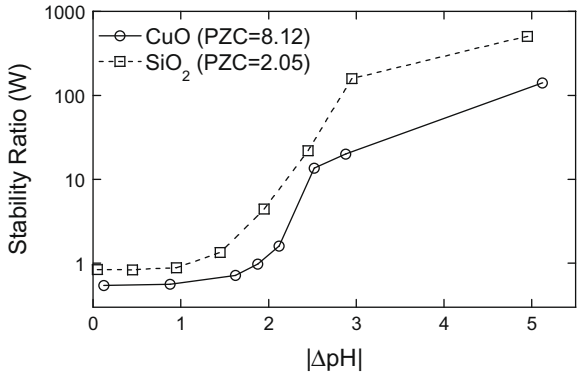

Fig. 5. Stability ratio of the two model systems as a function of |ΔpH| defined by |pH − PZC|.

U^{el} in most region of x, so that the negative U^{vdW} gives rise to a limited effect only very near the particle surface. In contrast, when U^{el} decreases gradually as pH approaches PZC, the x region affected by the U^{vdW} becomes broadened, resulting in a gradual increase in the value of x_{max}. Likewise, in the SiO_2–water system having a smaller Hamaker constant, the x_{max} is momentarily expected to appear closer to the particle surface, which is confirmed in Fig. 4b.

The stability of a colloid can be characterized by a dimensionless factor, the so-called stability ratio, W, which is defined by the ratio of "number of collisions between particles" to "number of effective collisions that result in coagulation" [1]. Large W denotes a stable colloidal system where only a fraction, $1/W$, of collisions are successful to cause a coagulational growth. From this regard, the reciprocal value of W has been interpreted as a sort of probability for the effective coagulation event, i.e. the sticking probability P_{ij} [11,36,37]. As the stability ratio W has been estimated from phenomenological coagulation rates determined by turbidity measurement, low angle light scattering and dynamic light scattering [1,38], it should be noted that the W does not say what happens in a microscopic level. Sun et al. [38] attempted to directly measure the sticking probability P_{ij} in the microscopic level by inducing a collision between two approaching particles in an optical trap (tweezer) and observing if the collision led to a permanent doublet. They showed that the micro-scale value of P_{ij} was in a very good agreement with the macro-scale value of $1/W$. Fuchs derived a general relationship of the W to the U_{tot} for equal-size particles in suspension as [1,27,28,37]

$$W = 2r\int_0^\infty \frac{\exp[U_{tot}(x)/k_bT]}{(x+2r)^2}dx = \frac{1}{P_{ij}} \quad (13)$$

Hence, Eq. (13) gives an important relation between P_{ij} or W and experimental process parameters through the interaction potential, U_{tot}. The value of W is obtained by conducting a numerical integration for Eq. (13) and is shown in Fig. 5 as a function of pH for both systems. Verwey and Overbeek (1948) [1] showed that the W was determined almost entirely by the value of maximum energy barrier $U_{tot,max}$. This is hardly surprising because $U_{tot}(x)$ enters the integrand through an exponential function. The ratio W can be therefore approximated by the value of $\exp(U_{tot,max}/k_bT)$. Recalling Fig. 4 where $U_{tot,max}$ in the SiO_2 system is higher than that in the CuO system at equal values of pH, the SiO_2 system should exhibit a higher value of W or a better stability than the CuO system, as shown in Fig. 5.

3. Monte Carlo simulations

Three-dimensional off-lattice Monte Carlo simulations are utilized to simulate irreversible aggregation in the two model systems

at different pHs. It is noted that the effect of either pH or any other systematic parameter can be realized in the MC simulations only through the stability ratio W or its reciprocal value P_{ij} (see Eq. (13)). Moreover, irreversible aggregation implies that every "effective" collision event generates a permanent inter-particle bonding. In this study, neither bond breakage nor restructuring of aggregates [16,17,39] is considered.

The algorithm for the MC simulation is depicted in Fig. 6. The simulation starts with N_T non-overlapping identical spherical particles distributed randomly in a cubic box with edge length of L. Here L is determined through the definition of the volume fraction of the particles (ϕ) in the box: $\phi = N_T\, v_p/L^3$ where v_p denotes the volume of a single primary particle as $v_p = \pi/6\, d_p^3 = 4\pi/3\, r^3$. Therefore, increasing N_T represents larger size of the box (L) at a constant ϕ. The volume fraction, ϕ, is set to 5×10^{-4} at which the ζ potential was experimentally measured. A periodic boundary condition is applied to all boundaries [13,16–18]. As a first step, a particle or aggregate (also referred to as cluster) is randomly chosen and then diffuses to random directions in a constant MC time step (set to a thousandth of characteristic collision time, typically <1 μs). The diffusion displacement Δs is set to a maximum allowable distance below which the resultant fractal dimension (d_f) exhibits a negligible variation. A series of MC simulations with various trials of Δs verified that the radius of the primary particle is a good choice, which was also confirmed by others [16].

Note in Fig. 6 that particle diffusion takes place conditionally only when the diffusion probability P_{diff} is larger than a random number drawn between 0 and 1. P_{diff} is defined by the ratio of diffusion coefficient D_i of the selected particle to that of the smallest particle in the box, i.e., the maximum diffusion coefficient $D_{\max}$ at that time. This condition allows smaller particles to have more chances to move, reflecting the faster diffusion of these particles. The diffusion coefficient D_i is estimated by the modified Stokes Einstein relation as $D_i(m_i) \propto m_i^{-1/df}$ where m_i is the mass of the selected particle or aggregate [13,15,40,41]. It should be recalled from Fig. 4 that the maximum energy barrier appears in very short range from the surface (at $x_{\max}$ = 1–8 nm) in most conditions. At the present volume fraction of particles (0.00054), the inter-particle separation is estimated to ca. 250 nm, two orders of magnitude larger than the $x_{\max}$. This suggests two important things that will greatly reduce the calculation time as compared to Brownian dynamics simulation: (1) Brownian random motion of particles is hardly affected by the interaction potential unless particles approach very closely and (2) the interaction between two aggregates is most likely dominated by the two closest primary particles existing at each end of the aggregate. Thus, the P_{ij} (or W shown in Fig. 5) is assumed to be constant during aggregation process at each pH condition.

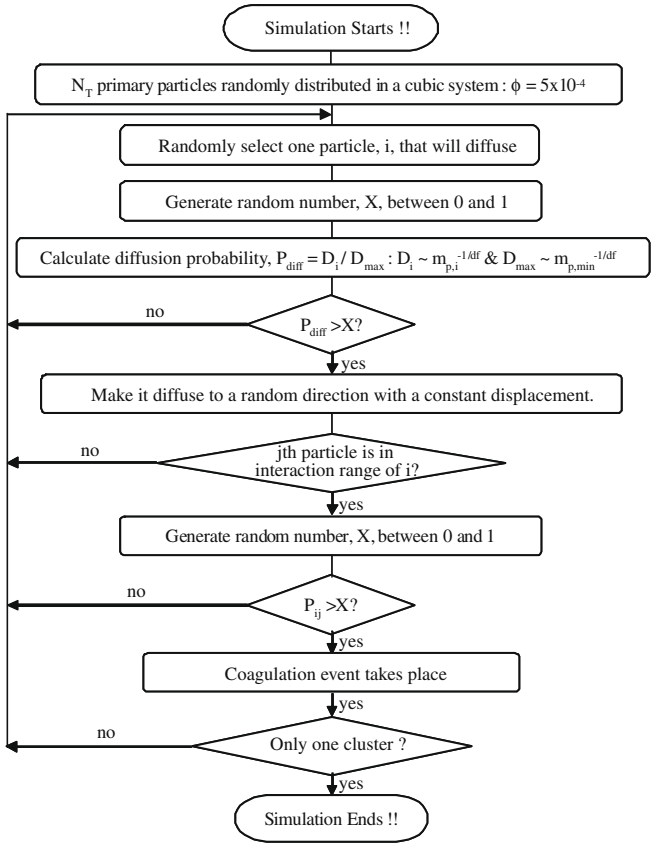

Fig. 6. Algorithmic flow chart of three-dimensional off-lattice Monte Carlo simulations.

While particles are moving in this way, the closest surface-to-surface distance is monitored at each MC step. When a pair of particles approach within 10% of primary particle diameter (0.1 d) [16], the pre-determined sticking probability P_{ij} as described in the previous section is used to determine whether or not an aggregation event takes place; when a randomly-drawn number between 0 and 1 is smaller than the P_{ij}, those two particles stick together. Moreover, applying two different values of the distance (0.1 d and 1.0 d) to DLCA and RLCA regimes, we confirmed that the resultant d_f were almost invariant. Finally, in any aggregation event, if a particle diffuses too closely to another particle so that they are overlapped, the approaching particle is set to move back in a way that the particles make a point contact. The simulation process is repeated until only one big aggregate remains in the box. The computational time varies depending on N_T, the sticking probability (P_{ij}), and diffusion displacement (Δs). In the present simulation condition (N_T = 2000, d_p = 25 nm, $\phi = 5 \times 10^{-4}$), the typical calculation time ranges from ~3 h to 4 days at most while P_{ij} varies from unity (DLCA) to 0.001 (RLCA), respectively.

4. Results and discussion

4.1. Effect of pH on microstructure of aggregates

In Sections 2 and 3, we described how pH, as a key parameter, was introduced to the MC simulations via the surface charge-induced potential, and the resultant stability ratio. Of particular interest in this section is to visualize structural changes of aggregates with changing pH by using the MC simulations. Figs. 7 and 8 shows representative images of the final aggregates resulting from two thousand, 25 nm diameter primary particles at the specified values of pH for CuO– and SiO_2–water systems, respectively. In the case of CuO, Fig. 7a corresponding to the largest deviation of pH from PZC ($|\Delta pH|$ = 5.12) shows the most compact structure of the aggregate while Fig. 7c shows an open structure near PZC ($|\Delta pH|$ = 1.9). On the other hand, Fig. 7b reveals an intermediate structures at $|\Delta pH|$ = 2.5.

Likewise, as seen in Fig. 8, SiO_2 aggregates show a similar behavior as pH departs from PZC ($|\Delta pH|$ increases from 1.9 to 2.9). Thus, the pH, in the form of $|\Delta pH|$, gives rise to significant effects on aggregate structures in both systems. In comparing Figs. 7 and 8, the parametric effect of pH is somewhat different depending on materials. While both systems show similar structures at low $|\Delta pH|$ of ~1.9 (see Figs. 7c and 8a), Fig. 8b at $|\Delta pH|$ = 2.95 looks different from Fig. 7b at $|\Delta pH|$ = 2.5 and shows a more compact structure than Fig. 7a at $|\Delta pH|$ = 5.1 does. This is attributed to the fact that the stability ratio W determining the structure is not a sole function of $|\Delta pH|$, as confirmed by Fig. 5, but altered by other material-dependent parameters such as A_{132}, K_p, K_d, Γ_{tot} and so forth (refer to Section 2).

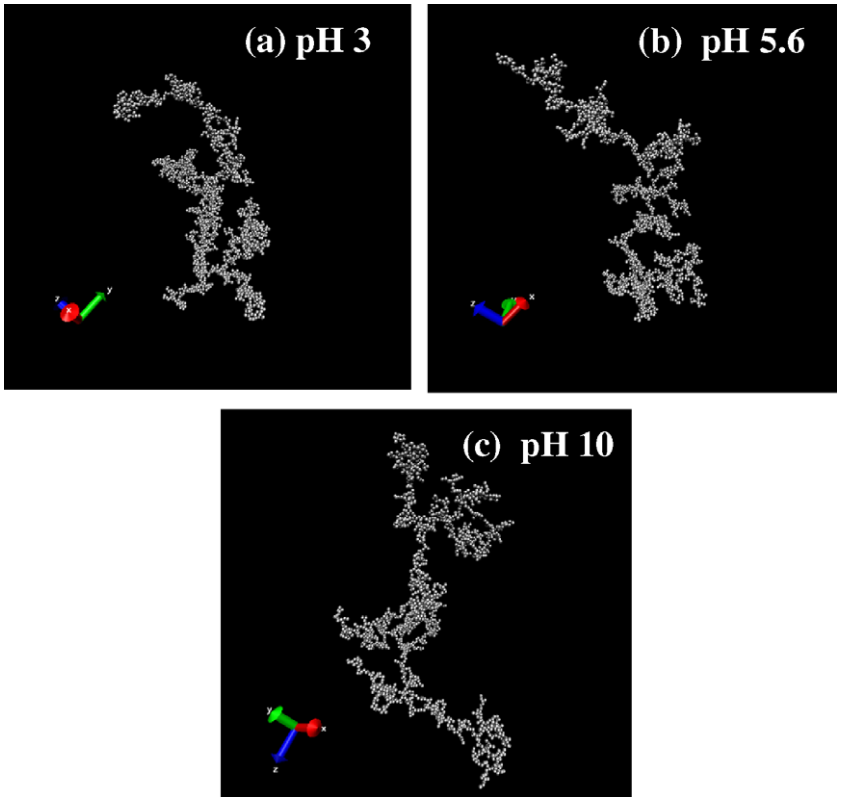

Fig. 7. Snapshots of CuO aggregates in water at various pHs.

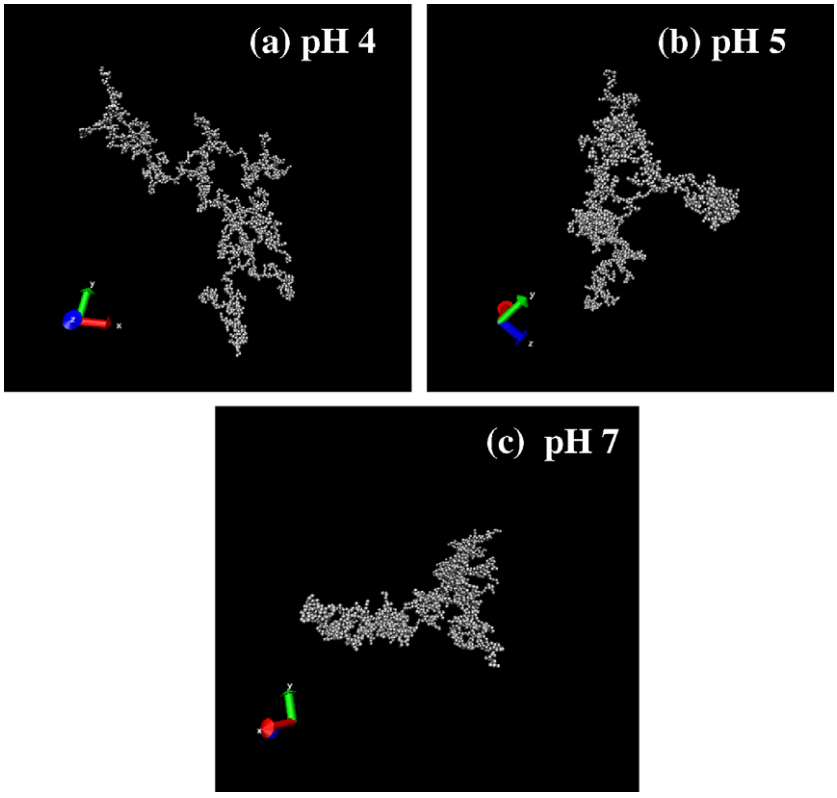

Fig. 8. Snapshots of SiO_2 aggregates in water at various pHs.

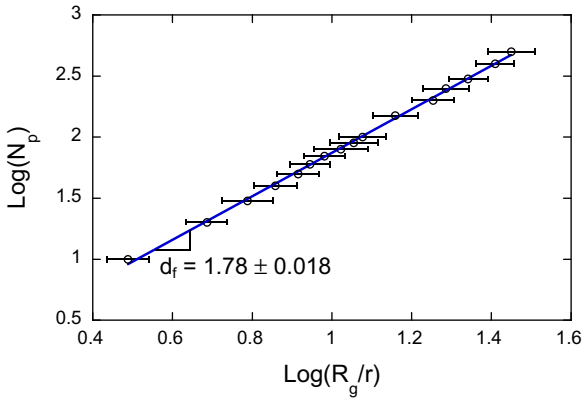

Fig. 9. Log–Log plot of mass vs radius of gyration of aggregates at $W = P_{ij} = 1$.

4.2. A correlation between fractal dimension and stability ratio

Fractal nature of aggregates is generally described by a power law as [5,7,8,13,15,16,24–27,41]

$$N_p = k_f (R_g/r)^{d_f} \tag{14}$$

where N_p is a number of primary particles comprising an aggregate, R_g is a radius of gyration, k_f is a prefactor in the order of unity, and r is a primary particle radius. While spherical monomer particles grow to form aggregates in a MC simulation, the fractal dimension d_f rapidly decreases from 3.0 to somewhere between 1.7 and 2.1 depending on the aggregation regime. Eq. (14) enables one to obtain a fractal dimension of a growing aggregate in the middle of the simulation, which was used for estimation of instantaneous value of the diffusion coefficient $D_i(m_i)$ (recall the Stokes Einstein relation) at any MC time steps. Alternatively, one may obtain a single fractal dimension from the slope of a log–log plot of N_p vs R_g for various sized aggregates.

Fig. 9 shows an example of the log–log plot for CuO at pH = 10 (equivalent to $W \approx 1$). A data point and its error bar in Fig. 9 denote an average and standard deviation of R_g from 50 runs of MC simulations for a constant number of primary particles N_T, respectively. This simulation is repeated for various initial numbers of the primary particles (from 10 to 2000) so as to obtain various sized aggregates. Note that these calculations give only a single value of d_f at a specific pH, so to get reasonable statistics each calculation is repeated 5–10 times for each pH and then the pH or W is varied. Such a high number of calculations likely provide a better statistical estimation of the fractal dimension. In this way, we obtained a relationship between d_f and pH as seen in Fig. 10. As expected from Figs. 7 and 8, the value of d_f obviously increases with increasing |ΔpH|, and follows a sigmoidal curve. The shape of the curve suggests three regions of |ΔpH| as noted in Fig. 10, i.e., the first region representing the nearly

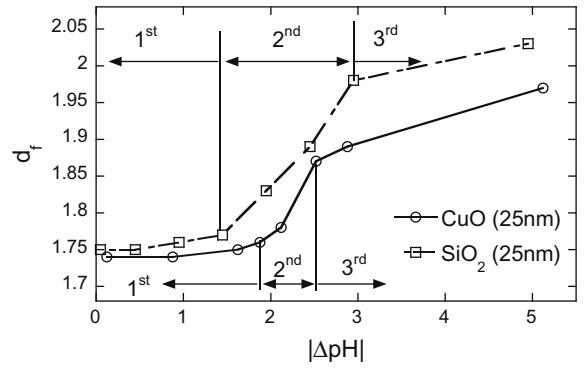

Fig. 10. Effect of pH on fractal dimensions of CuO and SiO_2 aggregates.

invariant d_f from 1.75, the transition region exhibiting a rapid change of d_f, and the near saturation region as the third. The value of $d_f \sim 1.75$ in the first region is in a good agreement with the literature value for the DLCA regime [11–18,21,24–26]. The third region showing the highest value of d_f in both systems likely corresponds to the RLCA regime of slow aggregation, though the d_f for both systems does not completely reach 2.1 representing the RLCA. Region two presumably corresponds to the transition from DLCA-to-RLCA.

Another thing to be noted is that the behavior is apparently material-dependent; the first region is bounded at different values of |ΔpH|, e.g., at |ΔpH| = ∼1.4 for SiO_2 system and at |ΔpH| = 1.9 for CuO systems, together with the different width of the 2nd region. In addition, SiO_2 aggregates show higher values of d_f than CuO over the entire range of |ΔpH|. These differences are readily understandable as long as one tries to interpret the horizontal axis |ΔpH| in conjunction with the corresponding values of W by using Fig. 5. For example, CuO at |ΔpH| ∼ 1.9 shows a nearly identical stability ratio to SiO_2 at |ΔpH| ∼ 1.0, and CuO at |ΔpH| ∼ 2.9 matches with SiO_2 at |ΔpH| ∼ 2.5 in this regard. This is exactly what we observed in Fig. 10. Overall, starting from Fig. 4, a higher repulsion barrier is developed an SiO_2 colloid due to stronger surface ionization, as well as a less attractive potential (see Fig. 3) even at the same |ΔpH|. This stabilizes the SiO_2 colloid more than CuO, leading to higher values of d_f.

In addition, it should be notable that the curves of d_f vs |ΔpH| in Fig. 10 show a very similar behavior to those in Fig. 5 (log(W) vs |ΔpH|), suggesting a strong correlation between d_f and log(W). This is confirmed by Fig. 11. Unlike the nonlinear sigmoidal profile of d_f vs |ΔpH|, the d_f is fairly well expressed by a linear function of log(W) as $d_f = 1.76 + 0.10 \log(W)$, which enables one to predict the final structure of aggregates from the stability ratio W or possibly from the pH using Fig. 5. In Fig. 11, the present correlation is also compared with preexisting correlations found by experiments [25,26]. Though all correlations are consistently linear, the slopes are somewhat different in such a way that the present correlation seems to agree better with the Berka and Rice's correlation [26]. Kim and Berg [25] measured aggregation kinetics of hydrophobic polystyrene latex spheres (PSL) in D_2O, while Berka and Rice [26] used hydrophilic clay mineral–water colloid. Given that metal oxide particles in this study are highly hydrophilic, the disagreement in the slope might be attributed to the differences in solvent affinity of colloidal particles. One might suggest that the present linear correlation be used only for metal oxide–water colloids.

4.3. An explicit correlation between fractal dimension and pH

Though we provide the correlations of d_f vs log(W) and W vs ΔpH, it can still be tedious to implement he model equation in Section 2. Here, the equations are revisited in efforts to draw their more explicit forms with a simplification, as well develop a new

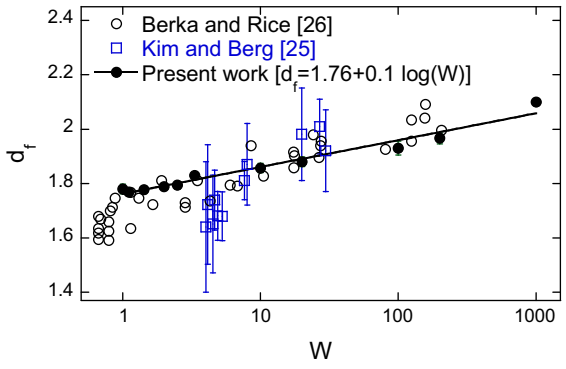

Fig. 11. A linear relation of fractal dimension to a log of stability ratio of colloidal aggregates.

parameter that solely relates to log(W). Through a course of simplifications for Eqs. (1)–(13), as described in Appendix, we obtained an approximated form of the maximum energy barrier $U_{tot,max}$ (see Eq. (A8)). According to Tsai et al. [6], the stability ratio W essentially scales as $\exp(U_{tot,max}/k_bT)$, leading to the relation of $\ln(W) = U_{tot,max}/k_bT$, which is consistent with Verwey and Overbeek (1948)'s suggestion [1] as discussed at the end of Section 2. Accepting this, we can finally derive an explicit relation between the parameters and the stability ratio W as

$$\ln(W) = \frac{U_{tot,\,max}}{k_bT} \approx \frac{1}{k_bT}\left(\frac{\alpha}{\kappa} - 2\sqrt{\alpha\beta}\right) \tag{15}$$

where α and β were defined in Eq. (A7), just for a simpler notation. In Eqs. (A8) and (15), the first term (α/κ) on the right was always larger than the second term of $2(\alpha\beta)^{1/2}$ by at least a factor of three when $1.0 \leqslant |\Delta pH| \leqslant 3.0$ for both systems. This suggests that the $\ln(W)$ can be approximated as $\sim f(\alpha/\kappa)$, implying that this parameter determines both the stability ratio of primary particles as well as the resultant structure of aggregates.

Given the above constraints and approximations we modify Fig. 5 by plotting the stability ratio vs α/κ rather than $|\Delta pH|$. The plot shown in Fig. 12a shows that both data sets collapse to a single sigmoidal curve implying that all material-dependent terms are adsorbed into α. Recalling the linear relationship of d_f vs $\log(W)$ in Fig. 10, we would expect another general relation of d_f vs α/κ to exist and this is shown in Fig. 12b. Note that all approximations underlying Eqs. (A1)-(A8) were only to draw out the functional form of the α, while the vertical data in $\log(W)$ in both Figs. 5 and 12a were calculated directly by using Eqs. (1)–(13) without any approximations.

We have so far dealt with inter-particle aggregation in liquids. In contrast, aggregation in gas phase is much simpler because the complexity arises from the surface charging of solid in liquid system which requires many complex parameters and calculations. Traditionally, aggregation in gas phase has been modeled as DLCA by setting the stability ratio W of unity. The only parameter that can alter the stability ratio in gas phase is surface charging, similar to in the present system. To deal with the effect in gas phase, one can just replace U_{tot} with conventional Coulomb potential in Eq. (13).

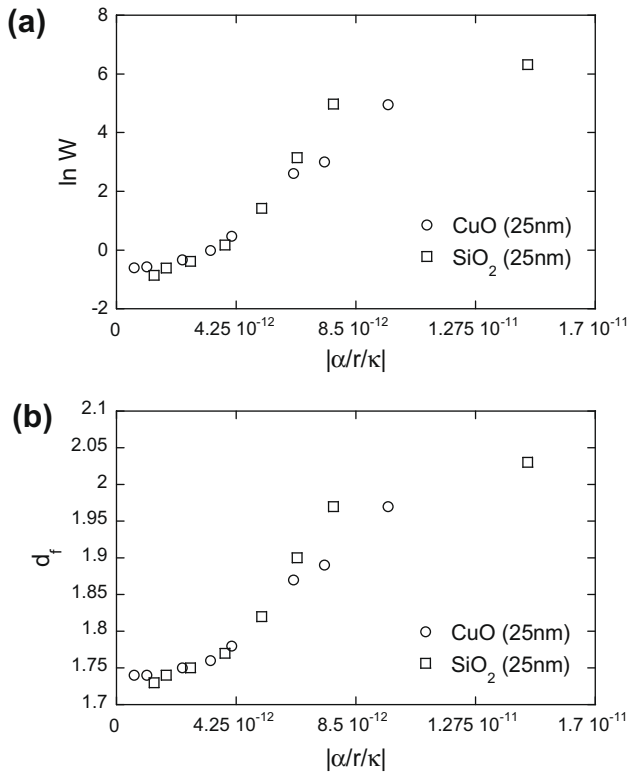

Fig. 12. Direct relations of: (a) stability ratio and (b) fractal dimension of the aggregates to the single incorporating parameter α.

5. Summary

In this study, we devoted to investigate the fundamental role of pH on microstructure of aggregates by incorporating colloidal science to Monte Carlo simulations. We chose water-based CuO and SiO_2 colloidal nanoparticles having totally different surface charging efficiencies as model systems. First, surface complexation model was used for best fitting the ζ potentials measured at various pHs, revealing other unknown parameters ahead being used to estimate surface charge potentials and stability ratio of colloidal particles. Plotting the stability ratio against $|\Delta pH| \equiv |pH - PZC|$ exhibited similar sigmoidal curves of the relation for two model systems that were divided into three distinct regimes such as DLCA limit, DLCA-to-RLCA transition, and RLCA limit. Monte Carlo simulations were performed at various pHs and revealed a linear relationship between the stability ratio of particles and fractal dimension of resultant aggregates which trend was consistent with previous experimental results. Nevertheless, the stability ratio was not a sole function of $|\Delta pH|$ but affected by other material-dependent ionization parameters such as Γ_{tot}, K_p, κ, and PZC, as well as physical parameters of particle radius and temperature. Developing a functional analysis, we successfully derived a new parameter incorporating all pre-mentioned parameters so that the stability ratio and fractal dimension were both expressed only by the single parameter.

Acknowledgment

This work was supported by the National Research Foundation of Korea (NRF) Grant funded by the Korea government (MEST) (No. 2009-0086170).

Appendix A

The first step to draw an explicit correlation between the stability ratio and experimental parameters is to make experimental parameters explicitly appear by converting Eq. (7) as

$$\begin{aligned}\sigma_0 &= F\Gamma_{tot}\frac{10^{-0.566\Delta pH} - 10^{0.566\Delta pH}}{10^{PZC}/K_P + (10^{-0.566\Delta pH} + 10^{0.566\Delta pH})} \\ &\approx \frac{F\Gamma_{tot}K_p}{10^{PZC}}[10^{-0.566\Delta pH} - 10^{0.566\Delta pH}]\end{aligned} \tag{A1}$$

where the denominator is dominated by the first term of $10^{PZC}/K_p$. Likewise, converting the implicit form of σ_β in Eq. (8), an explicit form of the net surface charge σ_s is derived from the sum of σ_0 and σ_β as

$$\begin{aligned}\sigma_s &= \frac{F\Gamma_{tot}}{10^{PZC}/K_P + (10^{-0.566\Delta pH} + 10^{0.566\Delta pH})} \\ &\quad\times\left[\frac{10^{-0.566\Delta pH}}{1 + K_a a(A^-)10^{-0.434\Delta pH}} - \frac{10^{0.566\Delta pH}}{1 + K_c a(C^+)10^{0.434\Delta pH}}\right] \\ &\approx \frac{F\Gamma_{tot}K_p}{10^{PZC}}\left[\frac{10^{-0.566\Delta pH}}{1 + K_a a(A^-)10^{-0.434\Delta pH}} - \frac{10^{0.566\Delta pH}}{1 + K_c a(C^+)10^{0.434\Delta pH}}\right]\end{aligned} \tag{A2}$$

If the association effect is neglected, the β-plane charge density σ_β arising from the association should be zero. In this regard, setting either $K_a = K_c = 0$ or $a(A^-) = a(C^+) = 0$ in Eq. (6), it is readily confirmed

that Eq. (A2) is reduced to Eq. (A1). Now, we have an explicit form of σ_s relating all experimental parameters denoting the material dependence. Recalling that Eq. (9) for charge balance offers a relationship between the potential ψ_d ($\approx \zeta$) and σ_s or σ_d, the potential ψ_d which will be fed to Eqs. (10)–(13) can be directly related to the parameters in Eq. (A2). Here, the following approximations are made for simplification, over the defined range of validity. The hyperbolic sine function in Eq. (9) is approximated to the square function $1.0517(F\psi_d/2RT)^2$ as

$$\sigma_s = -\sigma_d = -\frac{4000FI}{\kappa}\sinh\left(\frac{F\psi_d}{2RT}\right) \approx -\frac{1051.7\,F^3I}{\kappa R^2T^2}\psi_d^2 \tag{A3}$$

The maximum error of the approximation is revealed below 10% in the range of $F\psi_d/2RT \leqslant 3.0$ (corresponding to the DLCA and the transition regimes). As addressed, equating Eq. (A2) to Eq. (A3), the explicit functional form of ψ_d is given by

$$\psi_d^2 = \frac{\kappa R^2T^2\Gamma_{\mathrm{tot}}K_P}{1051.7IF^2 10^{PZC}}\left[\frac{10^{-0.566\Delta pH}}{1+K_a a(A^-)10^{-0.434\Delta pH}} - \frac{10^{0.566\Delta pH}}{1+K_c a(C^+)10^{0.434\Delta pH}}\right] \tag{A4}$$

Because the logarithmic function in Eq. (11) makes the following analysis difficult, we adopted a simpler form suggested at small potential as [1,6]

$$U^{el} = 2\pi\varepsilon_0\varepsilon_r r\psi_d^2\exp(-\kappa x) \tag{A5}$$

Substituting Eq. (A4) and the definition of κ to Eq. (A5), an explicit relation of U^{el} to the parameters is given as

$$U^{el} = \frac{3.803\pi rRT\Gamma_{\mathrm{tot}}K_P}{10^{PZC}\kappa} \times\left[\frac{10^{-0.566\Delta pH}}{1+K_a a(A^-)10^{-0.434\Delta pH}} - \frac{10^{0.566\Delta pH}}{1+K_c a(C^+)10^{0.434\Delta pH}}\right]\exp(-\kappa x) \tag{A6}$$

Applying Eqs. (12) and (A6) to Eq. (13), a simplified form of the U_{tot} is obtained by

$$U_{\mathrm{tot}} = \frac{3.803\pi rRT\Gamma_{\mathrm{tot}}K_P}{10^{PZC}\kappa} \times\left[\frac{10^{-0.566\Delta pH}}{1+K_a a(A^-)10^{-0.434\Delta pH}} - \frac{10^{0.566\Delta pH}}{1+K_c a(C^+)10^{0.434\Delta pH}}\right] \times\exp(-\kappa x) - \frac{A_{132}r}{12x} \equiv \frac{\alpha}{\kappa}\exp(-\kappa x) - \frac{\beta}{x} \approx \frac{\alpha}{\kappa}(1-\kappa x) - \frac{\beta}{x} \tag{A7}$$

where the exponential term of $\exp(-\kappa x)$ is approximated to $(1-\kappa x)$. Now, setting the first derivative of Eq. (A7) equal to zero ($dU_{\mathrm{tot}}/dx = 0$) gives the analytic solution of $x_{\max} = (\beta/\alpha)^{1/2}$. Since the term of $\kappa x_{\max}$ is always smaller than 0.4 in the present conditions, the approximation leads to an error of <10% Substituting $x_{\max}$ to Eq. (A7), an approximated form of the maximum energy barrier $U_{\mathrm{tot,max}}$ is eventually obtained as

$$U_{\mathrm{tot,\,max}} \approx \frac{\alpha}{\kappa}(1-\kappa x_{\max}) - \frac{\beta}{x_{\max}} = \frac{\alpha}{\kappa} - 2\sqrt{\alpha\beta} \tag{A8}$$

Here, the maximum error arising in the course of the above derivation processes was estimated up to 40%, mostly arising from the approximation in Eq. (A5).

References

[1] (a) R.J. Hunter (Ed.), Foundation of Colloid Science, first ed., Clarendon press, Oxford, 1987;
(b) E.J.W. Verwey, J.Th.G. Overbeek, Theory of Stability of Lyophobic Colloids, first ed., Elsevier, Amsterdam, 1948.
[2] D. Lee, S. Yang, M. Choi, Appl. Phys. Lett. 79 (2001) 2459–2461.
[3] S.E. Pratsinis, Prog. Energy Combust. Sci. 24 (1998) 197–219.
[4] D. Lee, M. Choi, J. Aerosol Sci. 31 (2000) 1145–1163.
[5] D. Lee, M. Choi, J. Aerosol Sci. 33 (2002) 1–16.
[6] D.-H. Tsai, R. Zangmeister, L. Pease, M.J. Tarlov, M.R. Zachariah, Langmuir 24 (2008) 8483–8490.
[7] D. Lee, Langmuir 23 (2007) 6011–6018.
[8] R. Prasher, P.E. Phelan, P. Bhattacharya, Nano Lett. 6 (2006) 1529–1534.
[9] M. Reim, W. Koerner, J. Manara, S. Korder, M. Srduini-Schuster, H.-P. Ebert, J. Fricke, Sol. Energy 9 (2005) 131–139.
[10] L. Mädler, A.A. Lall, S.K. Friedlander, Nanotechnology 17 (2006) 4783–4795.
[11] D. Fry, A. Chakrabarti, W. Kim, C.M. Sorensen, Phys. Rev. E 69 (2004) 61401-1–061401-9.
[12] A. Hasmy, J. Sol-Gel Sci. Technol. 15 (1999) 137–146.
[13] P. Meakin, J. Sol-Gel Sci. Technol. 15 (1999) 97–117.
[14] M. Lattuada, H. Wu, A. Hasmy, M. Morbidelli, Langmuir 19 (2003) 6312–6316.
[15] M. Lattuada, H. Wu, M. Morbidelli, J. Colloid Interface Sci. 268 (2003) 106–120.
[16] S.D. Orrite, S. Stoll, P. Schurtenberger, Soft Matter 1 (2005) 364–371.
[17] P. Meakin, Phys. Rev. Lett. 51 (1983) 1119–1122.
[18] J.C. Gimel, T. Nicolai, D. Durand, J. Sol-Gel Sci. Technol. 15 (1999) 129–136.
[19] Y. Efendiev, M.R. Zachariah, J. Colloid Interface Sci. 249 (2002) 30–43.
[20] G.C. Ansell, E. Dickinson, Phys. Rev. A 35 (1986) 2349–2352.
[21] M. Cerbelaud, A. Videcoq, P. Abelard, C. Pagnoux, F. Rossignol, R. Ferrando, Langmuir 24 (2008) 3001–3008.
[22] M. Lattuda, H. Wu, J. Sefcik, M. Morbidelli, J. Phys. Chem. B 110 (2006) 6574–6586.
[23] D.E. Rosner, R. McGraw, P. Tandon, Ind. Eng. Chem. Res. 42 (2003) 2699–2713.
[24] D. Asnaghi, M. Carpineti, M. Giglio, M. Sozzi, Phys. Rev. A 45 (1992) 1018–1023.
[25] A.Y. Kim, J.C. Berg, Langmuir 16 (2000) 2101–2104.
[26] M. Berka, J.A. Rice, Langmuir 21 (2005) 1223–1229.
[27] D. Lee, J.W. Kim, B.G. Kim, J. Phys. Chem. B 110 (2006) 4323–4328.
[28] N. Kallay, S. Zalac, Croat. Chem. Acta 74 (2001) 479–497.
[29] T. Kida, T. Oka, M. Nagano, Y. Ishiwata, X. Zheng, J. Am. Ceram. Soc. 90 (2007) 107–110.
[30] Q. Chen, L. Han, C. Gao, S. Che, Microporous Mesoporous Mater. 128 (2010) 203–212.
[31] I. Miletto, A. Gilardino, P. Zamburlin, S. Dalmazzo, D. Lovisolo, G. Caputo, G. Viscardi, G. Martra, Dyes Pigm. 84 (2010) 121–127.
[32] M. Kosmulski, J. Colloid, Interface Sci. 298 (2006) 730–741.
[33] J. Lyklema (Ed.), Fundamental of Interface and Colloid Science, Academic Press, London, 1991.
[34] R. Mueller, H.K. Kammler, K. Wegner, S.E. Pratsinis, Langmuir 19 (2003) 160–165.
[35] J.A. Lewis, J. Am. Ceram. Soc. 83 (2000) 2341–2359.
[36] M.Y. Han, H.K. Lee, Colloids Surf., A 202 (2002) 23–31.
[37] M. Mellema, J.H.J. van Opheusden, T. van Vliet, J. Chem. Phys. 111 (1999) 6129–6135.
[38] Z. Sun, S. Xu, G. Dai, Y. Li, Li Lou, Q. Liu, R. Zhu, J. Chem. Phys. 119 (2003) 2399–2405.
[39] P. Tandon, D.E. Rosner, J. Colloid Interface Sci. 213 (1999) 273–286.
[40] J.C. Gimel, D. Durand, T. Nicolai, Phys. Rev. B 51 (1995) 11348–11357.
[41] P. Meakin, Phys. Scr. 46 (1992) 295–331.